Charge fluctuations in a cluster Mott state: Hard x-ray photoemission study on a breathing kagome magnet Nb_3Cl_8

R. Nakamura,[1] D. Takegami,[2,1] K. Fujinuma,[1] M. Nakamura,[1] M. Ferreira-Carvalho,[2,3] A. Melendez-Sans,[2]
M. Yoshimura,[4] K.-D. Tsuei,[4] Y. Haraguchi,[5] H. Aruga Katori,[5] L. H. Tjeng,[2] and T. Mizokawa[1]
[1]*Department of Applied Physics, Waseda University, Shinjuku, Tokyo 169-8555, Japan*
[2]*Max Planck Institute for Chemical Physics of Solids, 01187 Dresden, Germany*
[3]*Institute of Physics II, University of Cologne, 50937 Cologne, Germany*
[4]*National Synchrotron Radiation Research Center, 30076 Hsinchu, Taiwan*
[5]*Department of Applied Physics and Chemical Engineering, Tokyo University of Agriculture and Technology, Tokyo 184-8588, Japan*

(Received 23 February 2024; revised 10 May 2024; accepted 23 July 2024; published 14 August 2024)

We report on our hard x-ray photoemission study of Nb_3Cl_8, wherein the breathing Kagome lattice of Nb provides interesting magnetic properties with spin 1/2 per Nb trimer. The Nb $3d_{5/2}$ and $3d_{3/2}$ core level peaks are accompanied by satellite peaks, suggesting the importance of Nb $4d$ charge degrees of freedom. The Cl $1s$ and $2p$ core level spectra have high binding energy peaks which can be assigned to the Cl site with Cl $3p$ ligand holes near the center of the Nb trimer. The core level spectra indicate that the Nb-Nb and Nb-Cl charge fluctuations play crucial roles in the magnetic interaction between the trimers.

DOI: 10.1103/PhysRevB.110.L081109

Introduction. Transition-metal compounds with partially filled t_{2g} orbitals often exhibit dimerization or trimerization of transition-metal ions due to the molecular orbital formation of the t_{2g} orbitals [1]. Examples include dimers formed in VO_2 [2,3] and $MgTi_2O_4$ [4,5]; trimers in $LiVO_2$ [6,7], $BaV_{10}O_{15}$ [8,9], and CsW_2O_6 [10,11]; and even octamers in $CuIr_2S_4$ [12,13]. The formation of such multimers in the partially filled t_{2g} level can be described by the orbitally induced Peierls mechanism [14,15]. In contrast to the multimer formation in the aforementioned transition-metal compounds, pairs along the c axis are already built in corundum-type Ti_2O_3 where Ti-Ti bond length is shortened below 450 K due to the molecular orbital formation by t_{2g} orbitals [2,16–18]. Very recently, Ti^{3+}/Ti^{4+} charge fluctuation of the Ti-Ti pair in Mg substituted Ti_2O_3 has been revealed by photoemission spectroscopy [19].

Mo trimers are naturally incorporated in the breathing Kagome layer of $LiZn_2Mo_3O_8$ and $Zn_2Mo_3O_8$ [20,21]. While the Mo valence is +4 with the t_{2g}^2 configuration in $Zn_2Mo_3O_8$, the average Mo valence in $LiZn_2Mo_3O_8$ is +3.67 with seven t_{2g} electrons per Mo trimer. The Mo trimers in $Zn_2Mo_3O_8$ are nonmagnetic since the six t_{2g} electrons fully occupy the three bonding molecular orbitals of the trimer. However, in $LiZn_2Mo_3O_8$, where the seven Mo $4d$ electrons are confined in the Mo trimer, each trimer can have localized spin 1/2. This situation can be viewed as a cluster Mott insulating state [22]. In $LiZn_2Mo_3O_8$, the localized spins of the Mo trimer form a geometrically frustrated triangular lattice providing the exotic spin liquid behavior [20,21]. Recently, Nikolaev, Solovyev, and Streltsov theoretically demonstrated that charge degrees of freedom allow a plaquette spin singlet state on the breathing Kagome lattice [23].

Nb_3Cl_8 is another striking Kagome system with Nb trimers as illustrated in Fig. 1(a) [24]. Such trimerization in the Kagome lattice with d^2 ions (such as Ti^{2+}, V^{3+}, and Nb^{3+}) would be explained by the orbitally induced Peierls mechanism. As shown in Fig. 1(b), one of the t_{2g} orbitals with yz, zx, or xy symmetry can form a quasi-one-dimensional band along one of the chain directions of the Kagome lattice. Since the one-dimensional band is half filled, each chain undergoes dimerization similar to VO_2. The dimers indicated by the thick lines in Fig. 1(b) can form the trimer with six t_{2g} electrons providing the nonmagnetic ground state. Indeed, $Na_2Ti_3Cl_8$ with Ti^{2+} undergoes Ti trimerization with suppression of magnetic susceptibility [26–30]. In Nb_3Cl_8, the Nb trimer accommodates one extra t_{2g} electron relative to the Ti trimer of $Na_2Ti_3Cl_8$ and hosts localized spin 1/2 [24,31,32]. When the transfer integrals between the neighboring Nb $4d$ orbitals in the trimer are much larger than those between the trimers, Nb_3Cl_8 can be viewed as a cluster Mott insulator and the Nb trimers form a triangular lattice, as proposed by Haraguchi *et al.* [32] and confirmed by Sun *et al.* and Gao *et al.* using angle-resolved photoemission spectroscopy (ARPES) [33,34]. The spin 1/2 triangular lattice of the cluster Mott insulating state is a new playground to study spin liquid states and exotic superconductivity [35,36]. Interestingly, Nb_3Cl_8 exhibits a further magnetic-nonmagnetic transition around 90 K, although degeneracy of orbital channel is already lifted. Haraguchi *et al.* proposed charge disproportionation between the trimers as an origin of the magnetic-nonmagnetic phase transition [32]. On the other hand, the recent ARPES work on $Nb_3Cl_6Br_2$ reported bonding-antibonding splitting of the lower Hubbard band [34], suggesting importance of hybridization between the trimers which can be mediated by the ligand orbitals.

Despite the highly interesting magnetic properties, fundamental electronic structure of Nb_3Cl_8 including the effect of ligand orbitals has not been clarified yet through bulk-sensitive core-level spectroscopy measurements. In this study, hard x-ray photoelectron spectroscopy (HAXPES) was

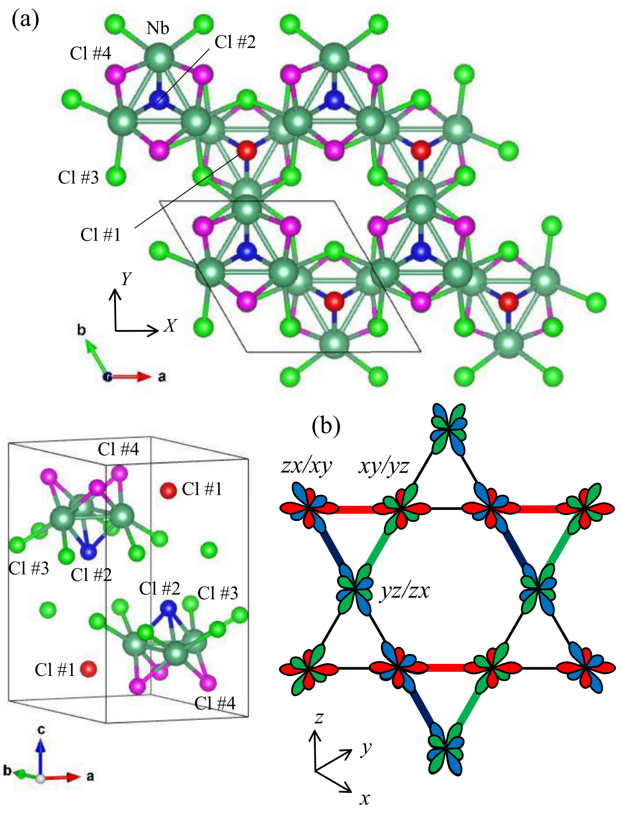

FIG. 1. (a) Crystal structure of Nb_3Cl_8 illustrated by VESTA [25]. (b) Possible orbital ordering for trimers formed by local d^2 ions.

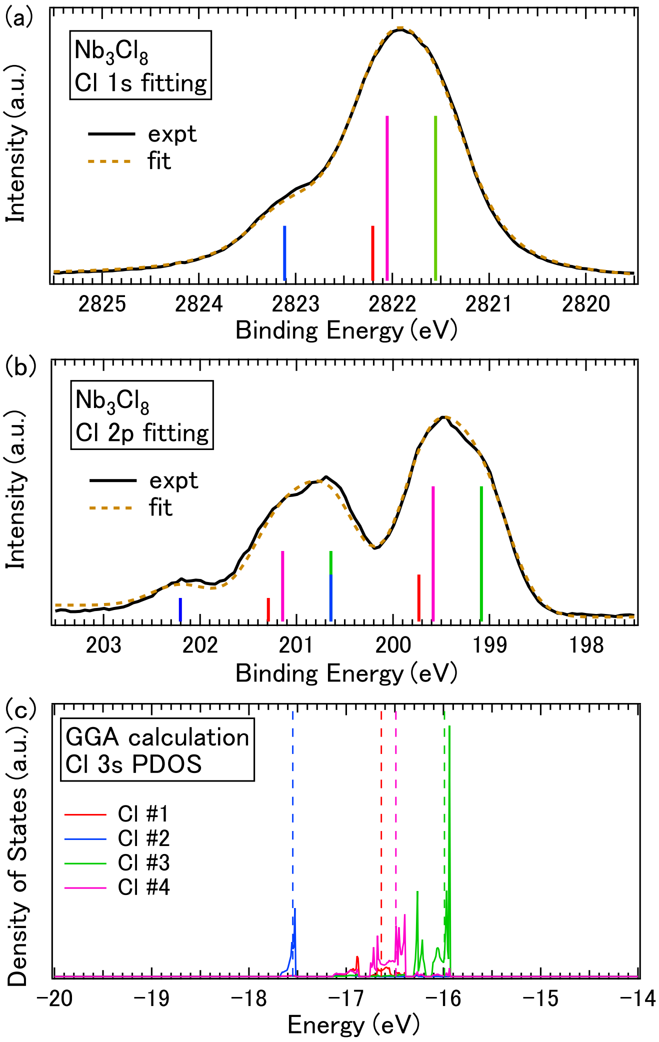

FIG. 2. (a) Cl 1*s* and (b) Cl 2*p* HAXPES spectra and the fitted results by using four Voigt functions and eight Gaussian functions, respectively, with the relative energy positions for Cl No. 1, No. 2, No. 3, and No. 4 obtained from the GGA calculation and the intensity ratio of 1:1:3:3. (c) Cl 3*s* partial density of states (PDOS) calculated by GGA. The PDOS is decomposed into contributions from the Cl No. 1, No. 2, No. 3, and No. 4 sites in Fig. 1(a). The center of gravity for each energy distribution is indicated by the vertical dashed bars for Cl No. 1, No. 2, No. 3, and No. 4.

performed on Nb_3Cl_8 to elucidate its unique electronic properties. The Nb 3*d* core-level HAXPES spectra indicate the importance of Nb 4*d* charge degrees of freedom. In addition, the Cl 1*s* and 2*p* core-level HAXPES spectra show that the Cl site just above/below the Nb trimer deviates from Cl^-, suggesting the Cl 3*p* state is involved in the charge excitation between the trimers.

Methods. HAXPES measurements were conducted at the Max-Planck-NSRRC HAXPES endstation [37], Taiwan undulator beam line BL12XU of SPring-8, with 6.5 keV photon energy. The probing depth is determined by the inelastic mean free path of the photoelectrons (with the kinetic energy of 5.5–6.5 keV) which is estimated to be about 4–5 nm in the universal curve [38] and is calculated to be about 10 nm for various inorganic compounds [39]. The x-ray incidence angle was 15 degrees with respect to the sample surface, and the photoelectron detection angle was 15 degrees off from the surface normal of the sample and parallel to the E vector of the x-ray. Single crystals were cleaved under ultrahigh vacuum of 10^{-6} Pa at 300 K to obtain clean sample surfaces as confirmed by survey scans (Fig. S1 in the Supplemental Material [40]). Since the sample was moderately charged up, the binding energy was corrected to set the lowest energy Nb 4*d* peak at ∼0.75 eV as reported in the ARPES studies [33,34]. After the correction, the Nb $3d_{5/2}$ peak is located at 204.8 eV which is close to the value report by Yoon *et al.* [41]. The measurements were performed at 300 K. The total energy resolution was about 300 meV. Generalized gradient approximation (GGA)-based band structure calculations were carried out using QUANTUM ESPRESSO 6.8 and 7.2 [42]. We employed pseudopotentials of Nb.pbe-spn-kjpaw_psl.1.0.0.UPF and Cl.pbe-n-kjpaw_psl.1.0.0.UPF, with the kinetic energy cutoff of 30 Ry and the charge density cutoff of 150 Ry.

Results. Figure 2(a) shows the experimental Cl 1*s* spectra (solid curve), revealing a prominent sharp peak accompanied by a second peak or shoulder approximately 1 eV higher in binding energy, constituting roughly one-eighth of the overall intensity. Figure 2(b) exhibits the experimental Cl 2*p* spectra (solid curve), where two primary peaks are observed, as expected from the $2p_{3/2}$ and $2p_{1/2}$ splitting. Additionally, a third smaller peak, roughly 1 eV higher in binding energy than the second peak, is evident. Notably, the main peaks for $2p_{3/2}$ and $2p_{1/2}$ show some finer structure. The presence of these extra peaks and the complex structure that the experimental Cl core levels display can be explained from the presence of four different Cl sites with significantly different environments. Figure 2(c) shows a close-up of the Cl 3*s* partial density of states (PDOS) obtained through *ab initio* GGA calculations, revealing significant differences in the PDOSs of the four Cl sites. The weights of the PDOS for each of the sites No. 1–No. 4 correspond to the ratio given by the multiplicity of each site (1:1:3:3). The PDOSs of sites No. 1, No. 3, and No. 4 located at higher energies (lower binding energy) exhibit broader features due to Cl-Cl band formations. In contrast, Cl No. 2, situated at the center of the trimers, has a significantly lower energy (higher binding energy) due to its stronger Nb-Cl hybridization with the trimer.

From these calculations, we use the center of masses of the PDOS of each of the Cl sites as an estimate of their on-site energy. To model the Cl 1*s* spectrum, we employ four Voigt functions (with common Gaussian and Lorentzian widths to account for experimental resolution and core-hole lifetime) with their energy separations obtained from the calculation for each Cl site and their intensity ratio of 1:1:3:3 corresponding to the site multiplicities. The simulation, depicted in Fig. 2(a), aligns well with the experimental data, demonstrating that the higher binding energy peak corresponds to the contributions of Cl No. 2. A similar approach is taken for the Cl 2*p* spectrum, utilizing four functions for the $2p_{3/2}$ and four more for the $2p_{1/2}$, split by the spin-orbit coupling and with the intensity ratio of 2:1. For the Cl 2*p*, the Lorentzian broadening was set to zero due to the longer core-hole lifetime. The results of the fit, shown in Fig. 2(b), agree closely with the experiments, revealing that the third peak originates from the Cl $2p_{1/2}$ of site No. 2, and that the fine structure observed in the main two peaks are due to the energy differences in site No. 3 and No. 4. The occupations of Cl 3*p* at Cl No. 1, No. 2, No. 3, and No. 4 are calculated to be 5.19, 4.96, 5.23, and 5.14. The number of Cl 3*p* holes of Cl No. 2 (at the center of the Nb trimer) is by 0.2–0.3 larger than the other Cl sites. Without trimerization, Cl No. 1 and No. 2 (No. 3 and No. 4) are equivalent, and the calculated Cl 2*p* spectra in an undistorted lattice fail to reproduce the experimental spectra as shown in Fig. S2 in the Supplemental Material [40]. In the literature, the Cl $2p_{3/2}$ peak is located around 199 eV for Cl^-, 206 eV for ClO_3^-, and 208 eV for ClO_4^- [43]. The Coulomb potential for the core level becomes deeper with less Cl 3*p* electrons due to stronger Cl 3*p*-Nb 4*d* hybridization or larger charge transfer from Cl 3*p* to Nb 4*d*. The Cl $2p_{3/2}$ peak for Cl No. 3 is located around 199.2 eV which is close to that of Cl^-, consistent with the weakest hybridization and the smallest charge transfer between Nb and Cl. On the other hand, the Cl $2p_{3/2}$ peak for Cl No. 2 is about 200.7 eV, indicating that number of Cl 3*p* electrons is considerably reduced due to the strong hybridization between Nb and Cl. Here, it should be noted that the surface-sensitive Cl 2*p* spectra with 240 eV photon energy reported in the Supplemental Material by Gao *et al.* [34] is largely different from those in the present HAXPES. This may indicate that the electronic structure of the surface layer is different from the bulk.

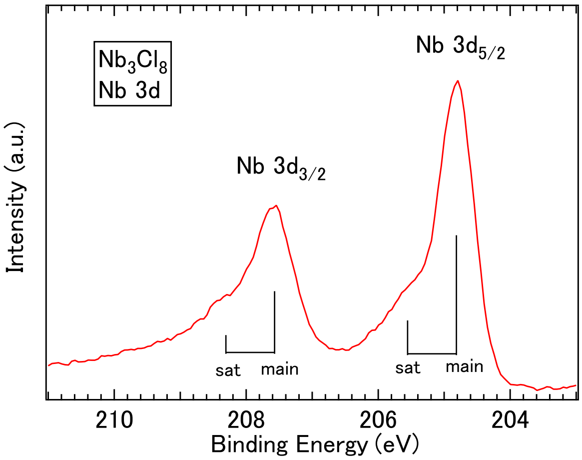

FIG. 3. Nb 3*d* HAXPES spectra with $h\nu = 6500$ eV for $\mathrm{Nb_3Cl_8}$. The Nb $3d_{5/2}$ and $3d_{3/2}$ main peaks are accompanied by satellite features.

As depicted in Fig. 3, the Nb 3*d* HAXPES peaks of the 5/2 and 3/2 branches are respectively accompanied by shoulders at the higher energy side. In various 4*d* and 5*d* transition-metal oxides (including $\mathrm{Ca_{2-x}Sr_xRuO_4}$ [44–47], $\mathrm{CaCu_3Ru_4O_{12}}$ [48–50], $\mathrm{Ba_{3-x}Sr_xNb_5O_{15}}$ [51,52], and $\mathrm{CsW_2O_6}$ [53]), such shoulder peaks and the main peaks are often observed and are attributed to the well and poorly screened final states. This screening arises from moderately correlated 4*d* or 5*d* electrons with relatively large band width. On the other hand, such screening effect is not available in $\mathrm{Nb_3Cl_8}$ which is a good insulator with a relatively large band gap. As shown in Fig. S3 in the Supplemental Material [40], the Nb 3*d* spectra of $\mathrm{Nb_3Cl_8}$ can be fitted by four Gaussians assuming main and satellite peaks for the 5/2 and 3/2 branches, and the area ratio of the satellite peak to the main peak is thus estimated to be about 1.0. It is tempting to assign the main and satellite peaks to the Nb^{2+} and Nb^{3+} states in the ground state since the formal valence of Nb is +2.67 in $\mathrm{Nb_3Cl_8}$. Since $\mathrm{Nb}^{2+} : \mathrm{Nb}^{3+} = 1:2$, as expected from the composition, and the core level binding energy of Nb^{3+} is higher than that of Nb^{2+}, the area ratio of the lower binding energy peak to the higher one should be 0.5. However, it can clearly be seen that the ratio significantly deviates from 0.5. In this context, the trimer in $\mathrm{Nb_3Cl_8}$ is different from the octamer of $\mathrm{CuIr_2S_4}$ [54] and the dimer of $\mathrm{LiRh_2O_4}$ [55] where the main and satellite peaks are assigned to different valence states.

Figure 4(a) shows the total DOS and PDOSs calculated by GGA for virtual structure with an undistorted Kagome lattice of Nb. The t_{2g} band represented by the $3Z^2 - R^2$ $((xy + yz + zx)/\sqrt{3})$ component mixed with XY and $X^2 - Y^2$ is distributed from −1.5 eV to 1.5 eV [The X and Y axes are indicated in Fig. 1(a)]. The t_{2g} band exhibits a finite energy gap around 0.2 eV due to the *xy*-*yz*, *yz*-*zx*, and *zx*-*xy* transfer integrals between the three Nb sites in the unit cell of the undistorted Kagome lattice. In this context, if all the Nb sites were 3+, the undistorted d^2 Kagome system would be a band insulator. Figure 4(b) displays the total DOS and PDOSs for real structures with a breathing Kagome lattice of Nb. The Nb 4*d* bands around 1 and 2 eV below the Fermi level have the character of bonding molecular orbitals in the Nb trimer. The 2 eV peak corresponds to the $1a_1$

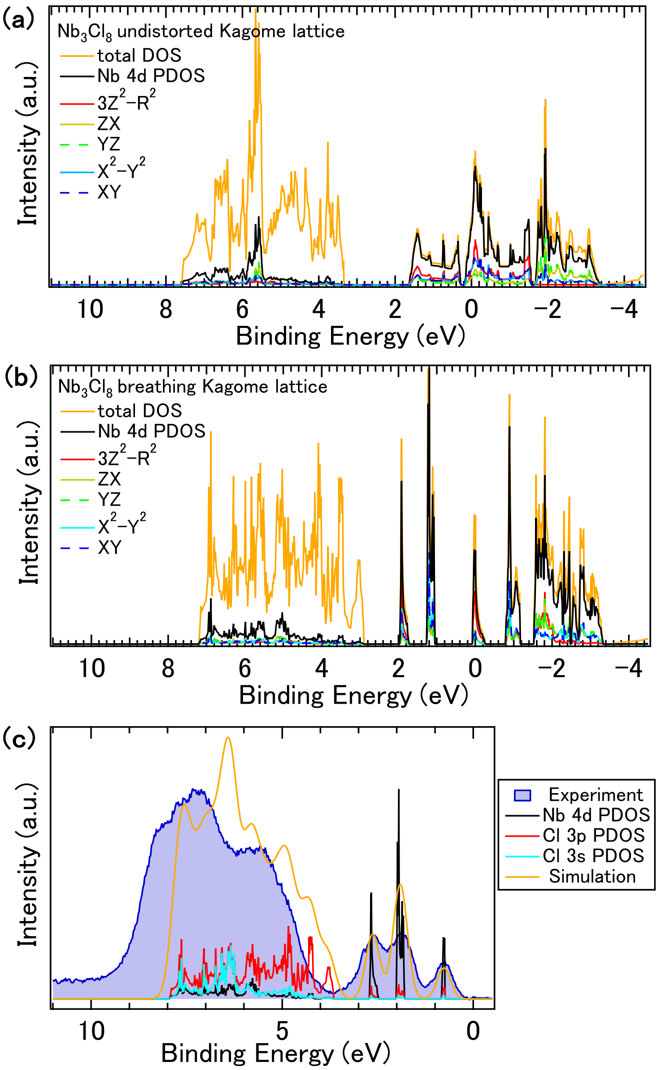

FIG. 4. Calculated density of states (DOS) and Nb 4d PDOS (a) for virtual structure with a regular Kagome lattice of Nb and (b) for real structure with a breathing Kagome lattice of Nb. The Nb 4d PDOS is decomposed into $3Z^2 - R^2$, ZX, YZ, $X^2 - Y^2$, and XY orbitals. (c) Valence-band HAXPES spectra with $h\nu = 6500$ eV of the Nb 4d and Cl 3p bands. The HAXPES spectra are compared with the simulated spectra which are obtained from the PDOS (below the Fermi level) for the real structure and the photoionization cross section of each subshell. The calculated density of states is broadened considering the energy resolution of 300 meV and shifted by 0.76 eV toward the lower energy (higher binding energy) side considering the Mott gap.

molecular orbital in the Nb trimer, accommodating two electrons per trimer. The 1 eV peak is derived from the 1e molecular orbitals which are doubly degenerate and accommodate four electrons per trimer. Since Nb_3Cl_8 has seven electrons per trimer in the Nb 4d states, the Fermi level is located at the Nb 4d band derived from the 2a_1 molecular orbital. The Nb 4d t_{2g} orbital component is redistributed by the trimerization, and the peak at the Fermi level is dominated by the $3Z^2 - R^2$ or a_{1g} orbital mixed with the e_g^π orbital.

In Fig. 4(c), the valence band spectra of Nb_3Cl_8 display the Cl 3p and Nb 4d states in the energy range from 4 to 9 eV and that from 1 to 4 eV, respectively. The Nb 4d states consist of the three peaks around 2.7, 1.9, and 0.7 eV. The 0.7 eV peak can be assigned to the 2a_1 molecular orbital of the trimer which is expected to be half-filled in the cluster Mott insulator state of Nb_3Cl_8. The half-filled 2a_1 states is split into the lower and upper Hubbard bands as theoretically demonstrated in the previous studies [34,56,57] as well as the GGA+U calculation shown in Fig. S6 of the Supplemental Material [40]. The simulated spectra obtained from the PDOSs calculated by GGA and the photoionization cross section [58,59] are compared with the experimental results. Here, we assume that the highest occupied band (2a_1) is half-filled and the entire spectrum is shifted to the lower energy (higher binding energy) due to the Mott gap. Except for the underestimation of the Cl 3p binding energy, the overall structure of the valence band HAXPES spectra is consistent with the calculated DOS.

Discussion. Considering the small band width of the half-filled band (2a_1) in the calculation shown in Fig. 4(b), it is plausible that relatively weak electron-electron interaction in the 2a_1 band may lead to opening of a Mott gap [35,36]. This aligns with the scenario of the cluster Mott insulator. If the Nb 4d electrons in the 2a_1 band are itinerant (namely, if the system is close to a metal-insulator transition), the Nb 3d core level spectra should exhibit well- and poorly screed features as seen in the undoped cases including $CaVO_3$ and Ca_2RuO_4 [60–63], and the doped cases including $Ba_3Nb_5O_{15}$ [51,52]. The absence of the well- and poorly-screed features in the Nb 3d core level spectra of Nb_3Cl_8 indicates that the Nb 4d electrons in the 2a_1 band are highly localized. In the ground state, the 2a_1 electron is evenly distributed among the three Nb sites, and it is trapped by the core-hole potential in the final states, giving rise to the main and satellite peaks in the Nb 3d core level spectra.

Examining the valence band spectra, the spectral weight ratio of the 1.9 eV peak (1e) to the 2.7 eV peak (1a_1) is expected to be two according to their degeneracy. However, in the experimental result, the 1.9 eV and 2.7 eV peaks are much wider than the simulation and exhibit comparable height, suggesting electronic correlation effect. When an electron is removed from the fully occupied 1a_1 or 1e orbitals, the remaining 1a_1 or 1e electrons can couple with the unpaired 2a_1 electron providing energy splitting. Since the energy splitting for 1e is larger than for 1a_1 due to its orbital degeneracy, the 1.9 eV peak can be much more strongly broadened. In addition, it is anticipated that the electron in the 0.7 eV peak (2a_1) is also correlated with the other Nb 4d electrons participating in the 1a_1 and 1e orbitals at each Nb site. Such correlation effect may drive the system toward a Nb^{2+}/Nb^{3+} mixed valence state if the Nb-Nb transfer integral is smaller than the multiplet coupling between the Nb 4d electrons. Moreover, the analysis of the Cl 1s and 2p spectra suggests importance of charge transfer from Cl to Nb. The Cl 3p PDOS in the valence band is plotted in Fig. S5 in the Supplemental Material [40]. The Cl 3p orbitals at the Cl No. 2 site are strongly hybridized into the unoccupied part of the Nb 4d band corresponding to 1a_2 and 3e. When the electron in 2a_1 is excited, the Cl 3p weight is redistributed and mixed into the final state with 2a_1 symmetry. The Nb-Nb and Nb-Cl fluctuations cause the plaquette-type magnetic coupling between the trimers [23], potentially leading to the magnetic-nonmagnetic transition at 90 K. Indeed, the bonding-antibonding splitting of the 2a_1

band reported by Gao *et al.* [34] is consistent with the singlet bond formation via the Nb-Cl charge transfer channel.

In summary, our investigation employed hard x-ray photoemission spectroscopy to explore the electronic structure of the breathing Kagome magnet Nb_3Cl_8. The Nb 3*d* core level spectra revealed main and satellite peaks, highlighting the significance of Nb 4*d* charge degrees of freedom and electronic correlation. Analysis of the Cl 1*s* and 2*p* core level spectra indicated the presence of a Cl 3*p* ligand hole at the Cl site just above/below the Nb trimer. These findings collectively suggest that the magnetic interaction between the spin 1/2 trimers is influenced by Nb-Nb and Nb-Cl charge fluctuations.

Acknowledgments. The authors would like to thank Prof. S.V. Streltsov for enlightening discussions. D.T. acknowledges the support by the Deutsche Forschungsgemeinschaft (DFG, German Research Foundation) under the Walter Benjamin Programme, Project No. 521584902. M.F.-C. greatly acknowledges funding from the German Research Foundation (DFG) Grant No. 387555779. The HAXPES measurements were facilitated by the Max Planck-POSTECH-Hsinchu Center for Complex Phase Materials. This work was supported by Grants-in-Aid from the Japan Society of the Promotion of Science (JSPS) (Grant No. JP22H01172).

[1] D. I. Khomskii, *Transition Metal Compounds* (Cambridge University Press, Cambridge, 2014).

[2] F. J. Morin, Oxides which show a metal-to-insulator transition at the Neel temperature, Phys. Rev. Lett. **3**, 34 (1959).

[3] M. W. Haverkort, Z. Hu, A. Tanaka, W. Reichelt, S. V. Streltsov, M. A. Korotin, V. I. Anisimov, H. H. Hsieh, H.-J. Lin, C. T. Chen, D. I. Khomskii, and L. H. Tjeng, Orbital-assisted metal-insulator transition in VO_2, Phys. Rev. Lett. **95**, 196404 (2005).

[4] M. Isobe and Y. Ueda, Observation of phase transition from metal to spin-singlet insulator in $MgTi_2O_4$ with $S = 1/2$ pyrochlore lattice, J. Phys. Soc. Jpn. **71**, 1848 (2002).

[5] M. Schmidt, W. Ratcliff, P. G. Radaelli, K. Refson, N. M. Harrison, and S. W. Cheong, Spin singlet formation in $MgTi_2O_4$: Evidence of a helical dimerization pattern, Phys. Rev. Lett. **92**, 056402 (2004).

[6] H. F. Pen, J. van den Brink, D. I. Khomskii, and G. A. Sawatzky, Orbital ordering in a two-dimensional triangular lattice, Phys. Rev. Lett. **78**, 1323 (1997).

[7] H. F. Pen, L. H. Tjeng, E. Pellegrin, F. M. F. de Groot, G. A. Sawatzky, M. A. van Veenendaal, and C. T. Chen, Phase transition in $LiVO_2$ studied by near-edge x-ray-absorption spectroscopy, Phys. Rev. B **55**, 15500 (1997).

[8] T. Kajita, T. Kanzaki, T. Suzuki, J. E. Kim, K. Kato, M. Takata, and T. Katsufuji, Opening of a charge gap with V trimerization in $BaV_{10}O_{15}$, Phys. Rev. B **81**, 060405(R) (2010).

[9] K. Takubo, T. Kanzaki, Y. Yamasaki, H. Nakao, Y. Murakami, T. Oguchi, and T. Katsufuji, Orbital states of V trimers in $BaV_{10}O_{15}$ detected by resonant x-ray scattering, Phys. Rev. B **86**, 085141 (2012).

[10] D. Hirai, M. Bremholm, J. M. Allred, J. Krizan, L. M. Schoop, Q. Huang, J. Tao, and R. J. Cava, Spontaneous formation of zigzag chains at the metal-insulator transition in the β-pyrochlore CsW_2O_6, Phys. Rev. Lett. **110**, 166402 (2013).

[11] Y. Okamoto, H. Amano, N. Katayama, H. Sawa, K. Niki, R. Mitoka, H. Harima, T. Hasegawa, N. Ogita, Y. Tanaka, M. Takigawa, Y. Yokoyama, K. Takehana, Y. Imanaka, Y. Nakamura, H. Kishida, and K. Takenaka, Regular-triangle trimer and charge order preserving the Anderson condition in the pyrochlore structure of CsW_2O_6, Nat. Commun. **11**, 3144 (2020).

[12] S. Nagata, T. Hagino, Y. Seki, and T. Bitoh, Metal-insulator transition in thiospinel $CuIr_2S_4$, Physica B **194-196**, 1077 (1994).

[13] P. G. Radaelli, Y. Horibe, M. J. Gutmann, H. Ishibashi, C. H. Chen, R. M. Ibberson, Y. Koyama, Y. S. Hor, V. Kirykhin, and S. W. Cheong, Formation of isomorphic Ir^{3+} and Ir^{4+} octamers and spin dimerization in the spinel $CuIr_2S_4$, Nature (London) **416**, 155 (2002).

[14] D. I. Khomskii and T. Mizokawa, Orbitally induced Peierls state in spinels, Phys. Rev. Lett. **94**, 156402 (2005).

[15] D. I. Khomskii and S. V. Streltsov, Orbital effects in solids: Basics, recent progress, and opportunities, Chem. Rev. **121**, 2992 (2021).

[16] L. L. Van Zandt, J. M. Honig, and J. B. Goodenough, Resistivity and magnetic order in Ti_2O_3, J. Appl. Phys. **39**, 594 (1968).

[17] H. Sato, A. Tanaka, M. Sawada, F. Iga, K. Tsuji, M. Tsubota, M. Takemura, K. Yaji, M. Nagira, A. Kimura, T. Takabatake, H. Namatame, and M. Taniguchi, Ti 3*d* orbital change across metal–insulator transition in Ti_2O_3: Polarization-dependent soft X-ray absorption spectroscopy at Ti 2*p* Edge, J. Phys. Soc. Jpn. **75**, 053702 (2006).

[18] C. F. Chang, T. C. Koethe, Z. Hu, J. Weinen, S. Agrestini, L. Zhao, J. Gegner, H. Ott, G. Panaccione, Hua Wu, M. W. Haverkort, H. Roth, A. C. Komarek, F. Offi, G. Monaco, Y.-F. Liao, K.-D. Tsuei, H.-J. Lin, C. T. Chen, A. Tanaka *et al.*, *c*-axis dimer and its electronic breakup: The insulator-to-metal transition in Ti_2O_3, Phys. Rev. X **8**, 021004 (2018).

[19] T. Miyoshino, D. Takegami, A. Meléndez-Sans, R. Nakamura, M. Yoshimura, K.-D. Tsuei, K. Takasu, T. Okuda, L. H. Tjeng, and T. Mizokawa, Intra *c*-axis dimer hybridization and mixed valency in Mg-doped Ti_2O_3, Phys. Rev. B **107**, 115145 (2023).

[20] J. P. Sheckelton, J. R. Neilson, D. G. Soltan, and T. M. McQueen, Possible valence-bond condensation in the frustrated cluster magnet $LiZn_2Mo_3O_8$, Nat. Mater. **11**, 493 (2012).

[21] M. Mourigal, W. T. Fuhrman, J. P. Sheckelton, A. Wartelle, J. A. Rodriguez-Rivera, D. L. Abernathy, T. M. McQueen, and C. L. Broholm, Molecular quantum magnetism in $LiZn_2Mo_3O_8$, Phys. Rev. Lett. **112**, 027202 (2014).

[22] G. Chen, H.-Y. Kee, and Y. B. Kim, Cluster Mott insulators and two Curie-Weiss regimes on an anisotropic kagome lattice, Phys. Rev. B **93**, 245134 (2016).

[23] S. A. Nikolaev, I. V. Solovyev, and S. V. Streltsov, Quantum spin liquid and cluster Mott insulator phases in the Mo_3O_8 magnets, npj Quantum Mater. **6**, 25 (2021).

[24] F. A. Cotton, M. P. Diebold, and W. J. Roth, Discrete trinuclear complexes of niobium and tantalum related to the local structure

in niobium chloride, Nb_3Cl_8, J. Am. Chem. Soc. **109**, 2833 (1987).

[25] K. Momma and F. Izumi, *VESTA* 3 for three-dimensional visualization of crystal, volumetric and morphology data, J. Appl. Crystallogr. **44**, 1272 (2011).

[26] D. J. Hinz, G. Meyer, T. Dedecke, and W. Urland, $Na_2Ti_3Cl_8$: From isolated Ti^{2+} ions to $[Ti_3]^{6+}$ clusters, Angew. Chem. Int. Ed. Engl. **34**, 71 (1995).

[27] N. Hänni, M. D. Frontzek, J. Hauser, D. Cheptiakov, and K. Kramer, Low temperature phases of $Na_2Ti_3Cl_8$ revisited, Z. Anorg. Allg. Chem. **643**, 2063 (2017).

[28] Z. A. Kelly, T. T. Tran, and T. M. McQueen, Nonpolar-to-polar trimerization transitions in the $S = 1$ kagome magnet $Na_2Ti_3Cl_8$, Inorg. Chem. **58**, 11941 (2019).

[29] A. Paul, C. M. Chung, T. Birol, and H. J. Changlani, Spin-lattice coupling and the emergence of the trimerized phase in the $S = 1$ kagome antiferromagnet $Na_2Ti_3Cl_8$, Phys. Rev. Lett. **124**, 167203 (2020).

[30] D. I. Khomskii, T. Mizokawa, and S. V. Streltsov, Comment on "spin-lattice coupling and the emergence of the trimerized phase in the $S = 1$ kagome antiferromagnet $Na_2Ti_3Cl_8$", Phys. Rev. Lett. **127**, 049701 (2021).

[31] M. Ströbele, J. Glaser, A. Lachgar, and H.-J. Meyer, Struktur und elektrochemische untersuchung von Nb_3Cl_8, Z. Anorg. Allg. Chem. **627**, 2002 (2001).

[32] Y. Haraguchi, C. Michioka, M. Ishikawa, Y. Nakano, H. Yamochi, H. Ueda, and K. Yoshimura, Magnetic-nonmagnetic phase transition with interlayer charge disproportionation of Nb_3 trimers in the cluster compound Nb_3Cl_8, Inorg. Chem. **56**, 3483 (2017).

[33] Z. Sun, H. Zhou, C. Wang, S. Kumar, D. Geng, S. Yue, X. Han, Y. Haraguchi, K. Shimada, P. Cheng, L. Chen, Y. Shi, K. Wu, S. Meng, and B. Feng, Observation of topological flat bands in the kagome semiconductor Nb_3Cl_8, Nano Lett. **22**, 4596 (2022).

[34] S. Gao, S. Zhang, C. Wang, S. Yan, X. Han, X. Ji, W. Tao, J. Liu, T. Wang, S. Yuan, G. Qu, Z. Chen, Y. Zhang, J. Huang, M. Pan, S. Peng, Y. Hu, H. Li, Y. Huang, H. Zhou *et al.*, Discovery of a single-band Mott insulator in a van der Waals flat-band compound, Phys. Rev. X **13**, 041049 (2023).

[35] Y. Zhang, Y. Gu, H. Weng, K. Jiang, and J. Hu, Mottness in two-dimensional van der Waals Nb_3X_8 monolayers (X=Cl, Br, and I), Phys. Rev. B **107**, 035126 (2023).

[36] J. Hu, X. Zhang, C. Hu, J. Sun, X. Wang, H.-Q. Lin, and G. Li, Correlated flat bands and quantum spin liquid state in a cluster Mott insulator, Commun. Phys. **6**, 172 (2023).

[37] J. Weinen, T. C. Koethe, C. F. Chang, S. Agrestini, D. Kasinathan, Y. F. Liao, H. Fujiwara, C. Schler-Langeheine, F. Strigari, T. Haupricht, G. Panaccione, F. Offi, G. Monaco, S. Huotari, K.-D. Tsuei, and L. H. Tjeng, Polarization dependent hard X-ray photoemission experiments for solids: Efficiency and limits for unraveling the orbital character of the valence band, J. Electron Spectrosc. Relat. Phenom. **198**, 6 (2015).

[38] M. P. Seah and W. A. Dench, Quantitative electron spectroscopy of surfaces: A standard data base for electron inelastic mean free paths in solids, Surf. Interface Anal. **1**, 2 (1979).

[39] H. Shinotsuka, S. Tanuma, C. J. Powell, and D. R. Penn, Calculations of electron inelastic mean free paths. XII. Data for 42 inorganic compounds over the 50 eV to 200 keV range with the full Penn algorithm, Surf. Interface Anal. **51**, 427 (2019).

[40] See Supplemental Material at http://link.aps.org/supplemental/10.1103/PhysRevB.110.L081109 for survey scan, Cl 2p simulation for virtual structure, Nb 3d fitting analysis, Nb 3p and Cl 2s spectra, GGA and GGA+U partial density of states.

[41] J. Yoon, E. Lesne, K. Sklarek, J. Sheckelton, C. Pasco, S. S. P. Parkin, T. M. McQueen, and M. N. Ali, Anomalous thickness-dependent electrical conductivity in van der Waals layered transition metal halide Nb_3Cl_8, J. Phys.: Condens. Matter **32**, 304004 (2020).

[42] P. Giannozzi, O. Andreussi, T. Brumme, O. Bunau, M. Buongiorno Nardelli, M. Calandra, R. Car, C. Cavazzoni, D. Ceresoli, M. Cococcioni, N. Colonna, I. Carnimeo, A. Dal Corso, S. de Gironcoli, P. Delugas, R. A. DiStasio Jr., A. Ferretti, A. Floris, G. Fratesi, G. Fugallo, R. Gebauer, U. Gerstmann, F. Giustino *et al.*, Advanced capabilities for materials modelling with Quantum ESPRESSO, J. Phys.: Condens. Matter **29**, 465901 (2017).

[43] S. Civiš, A. Knížek, P. B. Rimmer, M. Ferus, P. Kubelík, M. Zukalová, L. Kavan, and E. Chatzitheodoridis, Formation of methane and (per)chlorates on mars, ACS Earth Space Chem. **3**, 221 (2019).

[44] H.-D. Kim, H.-J. Noh, K. H. Kim, and S.-J. Oh, Core-level photoemission revealing the Mott transition, Phys. B: Condens. Matter **359-361**, 1267 (2005).

[45] Z. V. Pchelkina, I. A. Nekrasov, Th. Pruschke, A. Sekiyama, S. Suga, V. I. Anisimov, and D. Vollhardt, Evidence for strong electronic correlations in the spectra of Sr_2RuO_4, Phys. Rev. B **75**, 035122 (2007).

[46] G. Zhang and E. Pavarini, Mott transition, spin-orbit effects, and magnetism in Ca_2RuO_4, Phys. Rev. B **95**, 075145 (2017).

[47] A. Chikamatsu, Y. Kurauchi, K. Kawahara, T. Onozuka, M. Minohara, H. Kumigashira, E. Ikenaga, and T. Hasegawa, Spectroscopic and theoretical investigation of the electronic states of layered perovskite oxyfluoride $Sr_2RuO_3F_2$ thin films, Phys. Rev. B **97**, 235101 (2018).

[48] T. T. Tran, K. Takubo, T. Mizokawa, W. Kobayashi, and I. Terasaki, Electronic structure of $CaCu_3Ru_4O_{12}$ studied by x-ray photoemission spectroscopy, Phys. Rev. B **73**, 193105 (2006).

[49] T. Sudayama, Y. Wakisaka, K. Takubo, T. Mizokawa, W. Kobayashi, I. Terasaki, S. Tanaka, Y. Maeno, M. Arita, H. Namatame, and M. Taniguchi, Bulk-sensitive photoemission study of $ACu_3Ru_4O_{12}$ (A=Ca, Na, and La) with heavy-fermion behavior, Phys. Rev. B **80**, 075113 (2009).

[50] D. Takegami, C.-Y. Kuo, K. Kasebayashi, J.-G. Kim, C. F. Chang, C. E. Liu, C. N. Wu, D. Kasinathan, S. G. Altendorf, K. Hoefer, F. Meneghin, A. Marino, Y. F. Liao, K. D. Tsuei, C. T. Chen, K.-T. Ko, A. Günther, S. G. Ebbinghaus, J. W. Seo, D. H. Lee, G. Ryu *et al.*, $CaCu_3Ru_4O_{12}$: A high-Kondo-temperature transition-metal oxide, Phys. Rev. X **12**, 011017 (2022).

[51] T. Yasuda, Y. Kondo, T. Kajita, K. Murota, D. Ootsuki, Y. Takagi, A. Yasui, N. L. Saini, T. Katsufuji, and T. Mizokawa, Interplay between electronic correlation and atomic disorder in a low carrier density 4*d* transition-metal oxide, Phys. Rev. B **102**, 205133 (2020).

[52] R. Nakamura, T. Miyoshino, T. Kajita, T. Katsufuji, N. L. Saini, and T. Mizokawa, Electronic structure of $Ba_3Nb_5O_{15}$ and $Ba_2SrNb_5O_{15}$ studied by band calculation and photoemission spectroscopy, J. Phys. Soc. Jpn. **91**, 064711 (2022).

[53] R. Nakamura, D. Takegami, A. Melendez-Sans, L. H. Tjeng, M. Okawa, T. Miyoshino, N. L. Saini, M. Kitamura, D. Shiga, H. Kumigashira, M. Yoshimura, K.-D. Tsuei, Y. Okamoto, and T. Mizokawa, Electronic structure reconstruction by trimer formation in CsW_2O_6 studied by x-ray photoelectron spectroscopy, Phys. Rev. B **106**, 195104 (2022).

[54] K. Takubo, S. Hirata, J.-Y. Son, J. W. Quilty, T. Mizokawa, N. Matsumoto, and S. Nagata, X-ray photoemission study of $CuIr_2S_4$: Ir^{3+}-Ir^{4+} charge ordering and the effect of light illumination, Phys. Rev. Lett. **95**, 246401 (2005).

[55] Y. Nakatsu, A. Sekiyama, S. Imada, Y. Okamoto, S. Niitaka, H. Takagi, A. Higashiya, M. Yabashi, K. Tamasaku, T. Ishikawa, and S. Suga, Hard x-ray photoelectron spectroscopy of the metal-insulator transition in $LiRh_2O_4$, Phys. Rev. B **83**, 115120 (2011).

[56] S. Grytsiuk, M. I. Katsnelson, E. G. C. P. van Loon, and M. Rösner, Nb_3Cl_8: A prototypical layered Mott-Hubbard insulator, npj Quantum Mater. **9**, 8 (2024).

[57] A. Bouhmouche, A. Jabar, I. Rhrissi, and R. Moubah, Highly optical anisotropy, electronic and thermodynamic properties of the topological flat bands Kagome Nb_3Cl_8, Mater. Sci. Semicond. Process. **175**, 108238 (2024).

[58] J. J. Yeh and I. Lindau, Atomic subshell photoionization cross sections and asymmetry parameters: $1 \leqslant Z \leqslant 103$, At. Data Nucl. Data Tables **32**, 1 (1985).

[59] M. B. Trzhaskovskaya and V. G. Yarzhemsky, Dirac–Fock photoionization parameters for HAXPES applications, At. Data Nucl. Data Tables **119**, 99 (2018).

[60] K. Maiti, P. Mahadevan, and D. Das Sarma, Evolution of spectral function in a doped Mott insulator: Surface vs bulk contributions, Phys. Rev. Lett. **80**, 2885 (1998).

[61] K. Maiti, D. D. Sarma, M. J. Rozenberg, I. H. Inoue, H. Makino, O. Goto, M. Pedio, and R. Cimino, Electronic structure of $Ca_{1-x}Sr_xVO_3$: A tale of two energy scales, Europhys. Lett. **55**, 246 (2001).

[62] A. Sekiyama, H. Fujiwara, S. Imada, S. Suga, H. Eisaki, S. I. Uchida, K. Takegahara, H. Harima, Y. Saitoh, I. A. Nekrasov, G. Keller, D. E. Kondakov, A. V. Kozhevnikov, Th. Pruschke, K. Held, D. Vollhardt, and V. I. Anisimov, Mutual experimental and theoretical validation of bulk photoemission spectra of $Sr_{1-x}Ca_xVO_3$, Phys. Rev. Lett. **93**, 156402 (2004).

[63] R. J. O. Mossanek, M. Abbate, T. Yoshida, A. Fujimori, Y. Yoshida, N. Shirakawa, H. Eisaki, S. Kohno, P. T. Fonseca, and F. C. Vicentin, Electronic structure of the band-filling-controlled $CaVO_3$ and $LaVO_3$ compounds, J. Phys.: Condens. Matter **22**, 095601 (2010).